Vesicular instabilities: The prolate-to-oblate transition and other shape instabilities of fluid bilayer membranes

Marija Jarić,[1] Udo Seifert,[2] Wolfgang Wintz,[2,3] and Michael Wortis[1]

[1] *Physics Department, Simon Fraser University, Burnaby, British Columbia, Canada V5A 1S6*
[2] *Max-Planck-Institut für Kolloid- und Grenzflächenforschung, Kantstrasse 55, 14 513 Teltow-Seehof, Germany*
[3] *Institut für Festkörperforschung, Forschungszentrum Jülich, 52425 Jülich, Germany*
(Received 25 July 1995)

The equilibrium shapes of fluid-phase phospholipid vesicles in an aqueous solution are controlled by bending elasticity. The regime of nonvesiculated shapes at reduced volume $v \geq 1/\sqrt{2}$ involves the interplay of five branches of distinct stationary shapes: pears, prolates, oblates, stomatocytes, plus a branch of nonaxisymmetric shapes with the symmetry D_{2h}. We exploit a method for calculating explicitly the stability of arbitrary axisymmetric shapes to map out in a numerically exact way both the stable phases and the metastability of the low-lying shape branches. To obtain additional required information about nonaxisymmetric shapes, we calculate these by numerical minimization of the curvature energy on a triangulated surface. Combining these two methods allows us to construct the full (shape) phase diagram and the full stability diagram in this region. We provide explicit results for values of the bending constants appropriate to stearoyl-oleoyl-phosphatidylcholine; generalization to other values is straightforward.

PACS number(s): 87.10.+e, 68.10.−m, 82.70.−y

I. INTRODUCTION

Fluid-phase phospholipid bilayer vesicles of spherical topology are observed to exhibit a variety of shapes [1–9]. Many shape classes were originally identified in a seminal theoretical paper by Deuling and Helfrich [10], based on the insight [11, 12] that bilayer curvature energy is a key component of the energy functional that controls vesicle shape. Shape classes include elliptical shapes (both prolate and oblate), exhibiting up-down (reflection) symmetry, and the corresponding shapes (usually referred to as "pears" and "stomatocytes") in which this symmetry is broken. There are also regions of the phase diagram in which nonaxisymmetric elliptical shapes of D_{2h} symmetry [3, 13] or even "starfish" with D_{nh} symmetry (including $n = 7$!) [14, 15] are known to be stable. Finally, there are regions where the lowest-energy shapes are "vesiculated," consisting of two or more of these elementary shapes attached at narrow necks [16, 17].

Shape transitions between these classes occur when the overall energy minimum shifts from one shape class to another as a function of some control parameter, such as the overall area A or volume V of the vesicle. These transitions are, in principle, only sharp at temperature $T = 0$; nevertheless, for typical phospholipid systems, the energy scale of the shape-energy "landscape" is appreciably larger than k_BT, so transitions are normally sharp and well defined. Transitions may generically be of two types: When the ground state bifurcates, the transition is "second order," and the vesicle shape changes continuously. When the transition occurs as a result of the crossing of two distinct levels, it is "first order," and the vesicle shape changes discontinuously. Metastability and hysteresis often occur at first-order transitions, because energy barriers are commonly appreciably larger

than k_BT. In this situation, the metastable shape will continue to be locally stable well beyond the nominal transition, up to a point where the energy barrier out of the local minimum becomes comparable to k_BT. This occurs at a "spinodal" bifurcation of the metastable state, where a fluctuation mode becomes "soft" [9].

The "phase" diagram of vesicle shape is defined by the locus of points where level crossings and bifurcations occur in the appropriate space of control parameters. Regions of this phase diagram have been explored theoretically over the last few years [3, 7, 13, 16, 18–20]. Other regions, especially those at low reduced volumes, remain difficult with our present theoretical and computational capabilities.

It is the purpose of this paper to exhibit the most complete and exact phase diagram yet available for vesicles with parameters relevant to recent stearoyl-aleoyl-phosphatidylcholine (SOPC) experiments [2, 8, 9] in the context of the so-called area-difference-elasticity (ADE) model [7, 19–21]. In particular, we will describe the neighborhood of the oblate-prolate transition and its connection to the region of nonaxisymmetric shapes (including associated spinodal instability boundaries) more completely and more exactly than has previously been possible.

Based on a technique developed by one of us for the treatment of Gaussian fluctuations subject to hard constraints [22], we have constructed a protocol [23] for testing the stability of axisymmetric shapes to perturbations of arbitrary symmetry. This allows us to establish cleanly for the first time the loci of instability of both oblates and prolates to nonaxisymmetric perturbations generally and, in particular, to those of D_{2h} symmetry, which play an important role around the point at which the prolate, oblate, and nonaxisymmetric phases meet. The only pre-

viously published work in this central region of the phase diagram is the important paper of Heinrich, Svetina, and Žekš [20], who expand in a basis of spherical harmonics about the sphere and then use a variational procedure to find stationary-energy shapes [24]. It was known on the basis of work by Seifert, Berndl, and Lipowsky [13] that there is a region of the phase diagram for which no axisymmetric shapes are stable and, indeed, these authors speculated that the shapes in this region were elliptical with three unequal axes. However, Ref. [20] established the existence of the low-lying D_{2h} branch and the manner in which it bifurcates from the axisymmetric branches.

A stability analysis cannot provide any information about the shape that replaces a locally unstable axisymmetric shape (other than its symmetry in the case of a continuous transition, as discussed below). At present, there is no algorithm for integrating the shape equations [25] for nonaxisymmetric shapes, and the only available procedure is brute-force energy minimization over a triangulated surface. The best version of this approach now uses up to 4000 grid points and is capable of finding many of the complex shapes that inhabit the regime of low reduced volume [26, 27]. However, the time required for high-precision data is almost prohibitive. In the present paper, we employ this method to calculate some selected nonaxisymmetric D_{2h} shapes and the transitions involving these shapes. By using these data together with that obtained from the stability approach, we obtain a detailed quantitative phase diagram.

In Sec. II, we remind the reader of the essential ingredients of the ADE model [7, 19–21] and how it may be solved for axisymmetric shapes. We include a brief discussion of the protocol for locating instabilities, which is based on a complete calculation at the Gaussian level of the static fluctuation spectrum of an arbitrary axisymmetric shape subject to constraints [22, 23] of fixed overall volume V and area A. We also give a brief comment on the shape-energy minimization routine that we used to calculate the nonaxisymmetric shapes. Section III presents our results for the phase diagram and its associated spinodals. It gives a careful discussion of the relevant global structure of the space of stationary states, including a description at the Landau-theory level of the important bifurcations.

II. BACKGROUND

A. The ADE model

The ADE model is defined by a functional [7],

$$W[S] \equiv \frac{\kappa}{2} \oint dA[C_1(\mathbf{r}) + C_2(\mathbf{r}) - C_0]^2$$
$$+ \frac{\bar{\kappa}}{2}\frac{\pi}{AD^2}(\Delta A[S] - \Delta A_0)^2, \qquad (1)$$

which expresses the dependence of the energy W of a vesicle on its shape S [28]. The first term is the local bending energy, which depends on the bending modulus κ and the spontaneous curvature C_0. $C_1(\mathbf{r})$ and $C_2(\mathbf{r})$ are the two principal curvatures at each point $\mathbf{r}$ of the surface, so that

$$H = \frac{1}{2}(C_1 + C_2) \qquad (2)$$

is the local mean curvature. The integral is over the entire vesicle surface. The second term represents the elastic energy cost of forcing the actual area difference,

$$\Delta A[S] = 2D \oint dA H(\mathbf{r}), \qquad (3)$$

between the two leaves of the bilayer to differ from its relaxed value [29] ΔA_0. $\bar{\kappa}$ is the so-called nonlocal bending modulus, and D is the thickness of the bilayer. κ and $\bar{\kappa}$ have units of energy. They are generically of the same order of magnitude [7], and we denote their dimensionless ratio, $\alpha \equiv \bar{\kappa}/\kappa$. The energy scales for changing overall area and volume are much larger than the energy scale κ, so we consider only shapes S of given A and V. Once A is fixed, it is convenient to define a length scale R_A based on the definition $A \equiv 4\pi R_A^2$ and to reexpress the problem in terms of dimensionless variables. Thus,

$$v \equiv 3V/4\pi R_A^3, \qquad (4)$$

$$c_0 \equiv R_A C_0, \qquad (5)$$

$$m[S] \equiv \Delta A/2DR_A, \qquad (6)$$

and

$$m_0 \equiv \Delta A_0/2DR_A \qquad (7)$$

are suitably reduced versions of the volume, spontaneous curvature, area difference, and relaxed area difference, respectively. In terms of these convenient variables, one finds

$$W[S] = \kappa \left(G[S] + \frac{\alpha}{2}(m[S] - \bar{m}_0)^2 + w_0 \right), \qquad (8)$$

where

$$G[S] \equiv \frac{1}{2} \oint dA(2H)^2 \qquad (9)$$

and

$$\bar{m}_0 \equiv m_0 + 2c_0/\alpha. \qquad (10)$$

The constant w_0, which is independent of S, can be ignored in determining shapes. Note that c_0 and m_0 appear only in the combination $\bar{m}_0$, which we shall refer to as the effective reduced area difference. At α fixed, v and $\bar{m}_0$ are the axes of the vesicle-shape phase diagram. Observe, finally, that $G[S]$ and $m[S]$ are invariant under both Euclidean transformations and scale changes, so shapes related by such transformations have the same energy in the context of the ADE model (at fixed $\bar{m}_0$). Solving the shape problem now involves finding the shapes S that make $W[S]$ stationary at fixed v (and $\bar{m}_0$). The variational problem,

$$\delta W[S] = \kappa \{\delta G[S] + \alpha(m[S] - \bar{m}_0)\delta m[S]\} = 0, \qquad (11)$$

at $\delta v = 0$, leads for axisymmetric geometries to a set of nonlinear equations originally formulated by Deul-

ing and Helfrich [10]. In general, there are several branches of solutions, which we distinguish where necessary by a superscript n. Thus, the solutions will be a set of shapes $S^{(n)}(\bar{m}_0, v, \alpha)$ with corresponding energies $W^{(n)}(\bar{m}_0, v, \alpha)$. The stationary shape with lowest overall energy is the appropriate thermodynamically stable state at $T = 0$. Other shapes that are locally stable may be observed in the lab as metastable states, provided that the associated energy barriers are sufficiently high on the scale of $k_B T$.

In the form Eq. (11), the problem is evidently self-consistent, in that the combination [30] $\alpha(m - \bar{m}_0)$, which enters the shape equations parametrically, depends on $m[S]$, which, in turn, can only be calculated from the solution S. In practice, this self-consistency can be circumvented by the following route [7]: $G[S]$ is independent of the control parameters α and $\bar{m}_0$. Thus, the overall variational problem (11) can be divided into two steps. In the first step, we find the stationary solutions of $\delta G[S] = 0$ at fixed v and fixed m (simultaneously). This is the so-called area-difference (ΔA) (or bilayer-couple) model [13, 19, 21] We denote its stationary shapes $T^{(n)}(m, \alpha, v)$, with corresponding values, $G[T^{(n)}] \equiv G^{(n)}(m, \alpha, v)$. We have machinery in place [23] for finding these solutions numerically for fixed α and v as functions of m. To complete the program, we need only to make $W[T^{(n)}]$ stationary with respect to the parameter m, i.e., to solve

$$\bar{m}_0(m) = m + \frac{1}{\alpha}\frac{\partial G^{(n)}(m)}{\partial m}, \qquad (12)$$

where we have suppressed functional dependence on the nonvarying parameters α and v. Whenever there is a solution $m_0(m)$ of Eq. (12), then the shape $S^{(n)}(\bar{m}_0) \equiv T^{(n)}(m)$ makes $W[S]$ stationary with $W^{(n)}(\bar{m}_0) = W[T^{(n)}(m)]$.

It will be important in what follows to understand the stucture of Eq. (12). Characteristically, the stationary shapes $T^{(n)}(m)$ exist only over some range of m values. Over this range, the right side of Eq. (12) is single valued and smooth. If the structure of the function $G^{(n)}(m)$ is such that the right side is monotonic, then any solution $\bar{m}_0(m)$ is unique, and there is at most a single stationary shape and a single energy $W^{(n)}(\bar{m}_0)$ for each value of $\bar{m}_0$. On the other hand, if the right side is not monotonic, then two or more values of m may correspond to the same value of $\bar{m}_0$, so that the function $W^{(n)}(\bar{m}_0)$ becomes multiple valued. In such a situation, the turning point, where $\partial^2 G^{(n)}/\partial m^2 = -\alpha$, becomes a cusp in $W^{(n)}(\bar{m}_0)$, as illustrated in Fig. 1. When this happens, the lower part of $W^{(n)}(\bar{m}_0)$ in the associated "wing structure" is typically locally stable (for reasons that will become clear in Sec. III), while the upper part is unstable. The cusp corresponds to a spinodal point, where a particular branch n goes from stable to unstable without symmetry change [13].

In practice, we have determined the energies of relevant axisymmetric stationary shapes by the procedure outlined above. The program calculates the stationary shapes $T^{(n)}(m)$ of the ΔA model along with the corresponding values of $G^{(n)}(m)$ and $\partial G^{(n)}/\partial m$ [31]. Then, Eq. (12) is solved for $\bar{m}_0$, and Eq. (8) provides the ener-
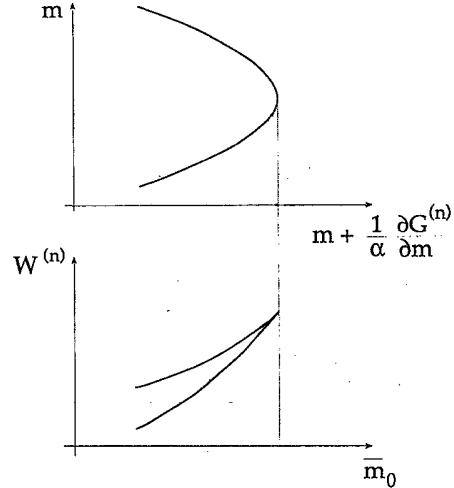

FIG. 1. Mechanism for the appearance of wing structure in $W(\bar{m}_0)$. The occurrence of a local extremum on the right-hand side of Eq. (12) produces a cusp in $W(\bar{m}_0)$ at the corresponding value of $\bar{m}_0$. The branch (n) changes stability at the cusp, as explained in the text. Wing structures of this type occur in pear, stomatocyte, and nonaxisymmetric branches.

gies $W^{(n)}(\bar{m}_0)$. The full energy-level diagram for axisymmetric branches is just the superposition of the energies $W^{(n)}(\bar{m}_0)$ for all distinct branches n. Any spinodal instabilities along a given branch n (i.e., those that do not involve a symmetry breaking) may be read off directly from the wing structures, as explained above. Instabilities involving the bifurcation of one axisymmetric branch from another are also directly visible on the energy-level diagram. What is missing at this point is all reference to nonaxisymmetric branches.

B. The Gaussian fluctuation spectrum for a vesicle of arbitrary shape subject to constraints

Vesicle-shape instabilities occur at soft-mode thresholds, i.e., when the energy of one (or more) of the physical fluctuation modes goes to zero. We sketch a formalism that we have developed [23] to calculate the fluctuation spectrum for a vesicle of arbitrary shape. We formulate the problem in general and comment briefly at the end on a few details of the implementation [23]. The approach taken here differs somewhat [32] from that taken in Ref. [22] and is closer in spirit to an earlier approach used by Peterson to determine the stability and fluctuations of oblates for $\alpha = 0$ and $\alpha = \infty$ [33]. At the level of practical implementation, this approach and that of Ref. [22] are, of course, identical.

Imagine that an equilibrium ($T = 0$) vesicle shape is given by $[S_0] \equiv \mathbf{R}_0(s_1, s_2)$, where (s_1, s_2) describes an appropriate set of coordinates on the two-dimensional surface. We represent an arbitrary small deformation of this surface as

$$[S] \equiv \mathbf{R}(s_1, s_2) = \mathbf{R}_0(s_1, s_2) + \epsilon(s_1, s_2)\mathbf{n}(s_1, s_2), \qquad (13)$$

where $\mathbf{n}(s_1, s_2)$ is the outward-pointing unit normal at the position (s_1, s_2). It is convenient to imagine that the magnitude of the displacement has been expanded in a complete set of real basis functions, $\epsilon_i(s_1, s_2)$, so

$$\epsilon(s_1, s_2) = \sum_i a_i \epsilon_i(s_1, s_2), \qquad (14)$$

with a_i real. The energy $W[S]$ of the deformed shape must be close to that of the equilibrium shape, so to quadratic order,

$$W[S] - W[S_0] = W_i a_i + \frac{1}{2} a_i W_{ij} a_j, \qquad (15)$$

where repeated-index summation will be understood henceforth. Although the deformation $\epsilon(s_1, s_2)$ is arbitrary, physical fluctuations must preserve the volume $V_0 \equiv V[S_0]$ and area $A_0 \equiv A[S_0]$ of the equilibrium shape. It follows that for physical fluctuations the set of coefficients $\{a_i\}$ must obey two constraints, which may be written, again, to quadratic order,

$$D^\alpha[S] - D^\alpha[S_0] = 0 = D_i^\alpha a_i + \frac{1}{2} a_i D_{ij}^\alpha a_j, \qquad (16)$$

where $\alpha = 1$ corresponds to the volume and $\alpha = 2$ to the area. It will be convenient in what follows to think of linear forms like $u = u_i a_i$ as the elements of a vector space.

Now, S_0 is a stationary shape, subject only to contraints on area and volume. Thus, the linear part of Eq. (15) can only refer to directions "along" the constraints and must, therefore, be a linear combination,

$$W_i a_i = \lambda^\alpha D_i^\alpha a_i, \qquad (17)$$

of the linear terms in the constraint equations (16). Indeed, with the usual identifications of the inside/outside pressure difference P [34],

$$\frac{\partial W[S^{(n)}]}{\partial V} = -P, \qquad (18)$$

and the surface tension Σ [34],

$$\frac{\partial W[S^{(n)}]}{\partial A} = -\Sigma, \qquad (19)$$

for any branch n of equilibrium shapes, we find $\lambda^{(1)} = -P$ and $\lambda^{(2)} = -\Sigma$. By substituting Eq. (17) into Eq. (15), we arrive at a purely quadratic form of the energy functional,

$$W[S] - W[S_0] = \frac{1}{2} a_i \Phi_{ij} a_j, \qquad (20)$$

where $\Phi_{ij} \equiv W_{ij} + PV_{ij} + \Sigma A_{ij}$ is called the "stability matrix" [34].

Equation (20) must, in principle, be used in connection with the full nonlinear equations (16), which serve to project out deformations that violate the constraints. However, in finding the Gaussian fluctuation spectrum, it suffices to deal with the constraints only at the linear level, since Eq. (20) is already quadratic. Thus, it

will be useful to project out of the problem the two-dimensional [35] subspace D spanned by the (linear) constraint vectors $d^\alpha = D_i^\alpha a_i$. The projection operator P_D onto this subspace may be constructed explicitly by using the Gram-Schmidt procedure to produce an orthonormal basis from the two vectors $\{d^\alpha\}$. We denote by Q the subspace (of codimension 2) of vectors orthogonal to the constraints, with its corresponding projection $P_Q = 1 - P_D$. The projected operator $P_Q \Phi P_Q$ is in general real symmetric, if the original basis $\{\epsilon_i\}$ has been chosen real. Thus, its eigenvectors, satisfying $P_Q \Phi P_Q v^\alpha = \omega^\alpha v^\alpha$, may be chosen to form a real orthogonal basis in Q. The set of (real) eigenvalues, $\{\omega^\alpha\}$, are the energies of the physical fluctuation modes. In this basis, we have by construction

$$W[S] - W[S_0] = \frac{1}{2} \omega^\alpha (v^\alpha)^2. \qquad (21)$$

Note that the six Euclidean operations automatically conserve area and volume, so the small deformations corresponding to these operations are automatically confined to the physical subspace Q. It follows that the physical fluctuation spectrum $\{\omega^\alpha\}$ will automatically include six zero eigenvalues (five for axisymmetric shapes S_0). It will be useful to denote the corresponding eigenvectors $\{e^\alpha\}$ and the six-dimensional (five-dimensional in the case of axisymmetric shapes) subspace that they span E, with projection P_E. The eigenvectors belonging to remaining eigenvalues, we denote $\{f^\alpha\}$. They define a subspace F, with projection P_F ($P_Q = P_E + P_F$). These eigenvalues reflect the local stability of the stationary shape S_0: If S_0 is locally stable, all the eigenvalues in F will be positive. If one (or more) of the eigenvalues in F is : .· ·. ·.·.. ·· ι S_0 is locally unstable in the corresponding ·· ·· ·· ·· ·, A locally stable state becomes unstable when one or more of the eigenvalues in F goes to zero as a function of the control parameters. Such a mode is called "soft," and its occurrence signals the onset of the physical instability of the constrained system.

We have at this point all the background needed for locating mechanical instabilities. It is worth noting, however, that Eq. (21) is the starting point for studying the statistics of Gaussian fluctuations about locally stable stationary shapes S_0 [22], i.e., those with $\omega^\alpha > 0$ for all α in F. In particular, at the Gaussian level, it suffices to define the thermal ensemble by integrating, $\prod_\alpha \int df^\alpha$, over the amplitudes $\{f^\alpha\}$ of the modes in F. The Euclidean modes correspond to rigid-body motions: They are neutral energetically and must be specifically excluded in discussion of the pure shape problem. The Gaussian integrals give $\langle f^\alpha \rangle = 0$ and

$$\langle f^\alpha f^\beta \rangle = \frac{k_B T}{\omega^\alpha} \delta_{\alpha\beta}, \qquad (22)$$

in the usual way. To return to the original variables, we must reexpand,

$$a_i = \sum_{\alpha \in D} c_i^\alpha d^\alpha + \sum_{\alpha \in F} c_i^\alpha f^\alpha. \qquad (23)$$

Note that the Euclidean modes have been explicity excluded from the sum [36]. Now, thermal fluctuations

must satisfy the constraints, so, at lowest order in the small parameters, $(k_B T/\omega^\alpha)^{1/2}$,

$$\langle a_i \rangle = \sum_{\alpha \in D} c_i^\alpha \langle d^\alpha \rangle = 0 + O(k_B T/\omega) \qquad (24)$$

and

$$C_{ij} \equiv \langle a_i a_j \rangle = \sum_{\alpha \in F} c_i^\alpha \frac{k_B T}{\omega^\alpha} c_j^\alpha$$

$$= k_B T \left[(1 - P_D - P_E) \Phi (1 - P_D - P_E) \right]_{ij}^{-1}. \qquad (25)$$

At the next higher order, however, nonlinear terms in the constraint equations come in, making $\langle d^\alpha \rangle \neq 0$, in general. Thus, taking the thermal average of Eq. (16) leads to

$$D_i^\alpha \langle a_i \rangle = \sum_{\beta \in D} D_i^\alpha c_i^\beta \langle d^\beta \rangle = -\frac{1}{2} C_{ij} D_{ij}^\alpha, \qquad (26)$$

which is of order $k_B T/\omega$. Inverting the two-by-two matrix, $H^{\alpha\beta} \equiv D_i^\alpha c_i^\beta$, evaluates

$$\langle d^\alpha \rangle = -\frac{1}{2} \sum_{\beta \in D} (H^{-1})^{\alpha\beta} C_{ij} D_{ij}^\beta \qquad (27)$$

and, correspondingly,

$$\langle a_i \rangle = -\frac{1}{2} \sum_{\alpha, \beta \in D} c_i^\alpha (H^{-1})^{\alpha\beta} C_{ij} D_{ij}^\beta, \qquad (28)$$

correcting Eq. (24) through order $k_B T/\omega$. The significance of Eqs. (27) and (28) is that they show how the constraints on V and A, in reducing the dimension of the space of physically allowed deformations, force thermal shifts into the problem, even at the Gaussian level [37].

In practice, for axisymmetric equilibrium shapes, the spherical harmonics $Y_{l,m}(\pi s/s^*, \phi)$ are a convenient basis, where s is the arclength measured from one pole, s^* is the overall pole-to-pole arclength, and ϕ is the azimuthal angle. The functions $Y_{l,m}$ are not real but satisfy $Y_{l,m}^* = (-1)^m Y_{l,-m}$, so, in order to have a real basis, it is necessary to form the linear combinations,

$$\eta_{lm}^{(+)} \equiv (Y_{lm} + Y_{lm}^*)/\sqrt{2} \qquad (29)$$

and

$$\eta_{lm}^{(-)} \equiv i(Y_{lm} - Y_{lm}^*)/\sqrt{2}. \qquad (30)$$

The deformations are then characterized by coefficients $\{a_i\}$ with the composite index $i \equiv \{m, \pm, l\}$ with $m \geq 0$, $l \geq m$, and $(-)$ missing for $m = 0$. Because of the axisymmetry, sectors with different m do not mix. Furthermore, for given m, the $(+)$ and $(-)$ sectors are independent and identical [except, of course, for $m = 0$ for which the $(-)$ sector is absent]. Thus, for all $m > 0$ the spectrum of eigenvalues $\{\omega^m\}$ is twofold degenerate. If, in addition, $[S_0]$ has up-down symmetry, then each m sector splits into subsectors of even and odd l.

The individual sectors now represent separate problems, and it is important to understand which sectors are affected by the constraints and by the Euclidean modes.

Perturbations with $m \neq 0$ enter the volume and area at most quadratically, so the constraint projection D lives entirely in the $m = 0$ sector [22]. The $m > 0$ sectors see the effect of the constraints only through the quadratic contributions, $D_{ij}^\alpha \rightarrow D_{mll'}^\alpha$, to the stability matrix (20); otherwise, they remain effectively unconstrained [22, 38]. For the five Euclidean modes, translation along the symmetry axis lives in the $m = 0$ sector; the two translation modes in directions perpendicular to the symmetry axis and the two rotation modes about such direction all live in the $m = 1$ sector [paired degenerately in $(+)$ and $(-)$]. When up-down symmetry is also present, the Euclidean modes are further localized: The $m = 0$ translation mode is in the odd-l subsector; the $m = 1$ translation modes are in the odd-l subsector; and, the $m = 1$ rotation modes are in the even-l subsector.

Because the $m = 0$ deformations are axisymmetric, the stability information that this sector contains is in principle already available by looking at the "wing" structures for the axisymmetric equilibrium shapes, as discussed at the end of Sec. II A. The remaining stability information, from the $m > 0$ sectors, does not involve the projection D and sees the constraints only through the (quadratic) contributions to the stability matrix, as discussed above.

C. Nonaxisymmetric shapes

Nonaxisymmetric shapes can be calculated by an approach developed by one of us [26, 27] based on a discretization of the curvature energy, mean curvature, area, and volume on a triangulated surface. The constraints are incorporated into the bending energy, Eq. (8), by adding appropriate quadratic terms with large coefficients (i.e., inverse "compressibilities," of the order of $\sim 10^5$). The resulting total "energy" is then minimized by a modified conjugate gradient algorithm. The resulting shape is a local energy minimum, which depends in principle on the initial shape chosen. Since we know the symmetry of the branches involved, this dependence on the initial shape causes no problems in the high-volume region considered here. Our algorithm differs from the related public domain "Surface Evolver" package of computer programs [39] in several respects, such as the discretization of the bending energy, the treatment of the constraints, and the minimization algorithm. In particular, we have taken special measures to prevent instabilities associated with tangential motion of vertices. These technical aspects will be discussed elsewhere [27].

We employ this algorithm to calculate axisymmetric and nonaxisymmetric shapes at $\alpha = \infty$ (in fact, $\alpha \sim 10^5$). Then, in a second step, we map the data to $\alpha = 1.4$, using the mapping described in Sec. II A. The advantage of this procedure is twofold: First, it turns out that the relaxation times are typically significantly smaller at $\alpha = \infty$ than at finite α of order one. Second and more importantly, a direct minimization yields only locally stable shapes but no stationary and unstable shapes. Often, however, stationary unstable shapes are the saddle points between locally stable shapes. Knowing these saddle points and their energy gives important

information about the activation barrier and the degree of hysteresis at a first-order transition. Since some of the nonaxisymmetric shapes that are stable at $\alpha = \infty$ turn into saddle points at lower values of α, we gain information on the activation barrier by calculating the corresponding shapes at $\alpha = \infty$ and then mapping to smaller α.

III. RESULTS

The principal results of this paper are contained in Figs. 2 and 3, the phase diagram and the stability diagram, respectively, which are discussed in the first two subsections below. A third subsection shows the results of direct, numerical minimization at a selected value of the reduced volume v. The final part of this section describes in some detail the bifurcation structures underlying these results.
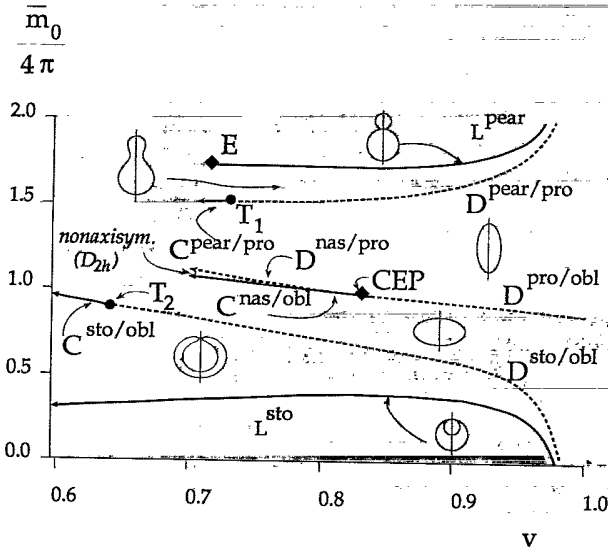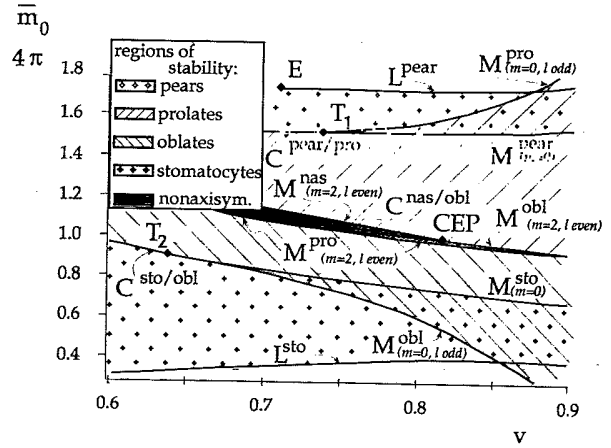

FIG. 3. Stability diagram of the ADE model for $\alpha = 1.4$ over the same region covered by Fig. 2. The textured areas identified by the key indicate the regions of local stability of the five phases shown. The limiting lines L and the continuous transitions C are the same as in Fig. 2. In addition, the spinodal lines M mark other limits of local stability. The various lines D are not shown; however, their location may be inferred: Thus, $D^{\text{pear/pro}}$ lies in the region between M^{pro} and M^{pear} emanating from T_1; $D^{\text{sto/obl}}$ lies in the analogous region emanating from T_2; $D^{\text{pro/obl}}$ lies between M^{obl} and M^{pro} to the right of CEP; and, $D^{\text{nas/obl}}$ lies in shaded nas region.

A. The phase diagram

The phase diagram plots the regions in $(v, \bar{m}_0)$ over which the lowest-energy, equilibrium shape belongs to each stationary branch n. Figure 2 shows the phase diagram of the ADE model for $\alpha = 1.4$ with reduced volume v in the range $0.6 < v < 1$ and for effective area difference $\bar{m}_0$ [Eq. (10)] near unity. Phase boundaries with $\bar{m}_0 > 4\pi$ have purposely not been shown for $v < 0.7$. This is because the line L^{pear} terminates at $v = 1/\sqrt{2}$ in a special point E, at which the radii of the two coexisting limiting spheres become equal. In the near neighborhood of E, other phases are known to occur [7]. Likewise, the nonaxisymmetric region (nas) has not yet been carefully studied below the cut at $v = 0.7$, which we have explored numerically (see Sec. III C).

The choice of α corresponds to the measured value for SOPC [7, 40]. Different lipids have different values of α [e.g., $\alpha \sim 1.1$ for di-myristoyl-phosphatidylcholine (DMPC) [7]], so in this sense the choice is somewhat arbitrary. On the other hand, the local structure of the phase diagram remains generic over a range of α, until the relevant bifurcation structures change. In any case, this phase diagram represents both a useful example and a feasibility proof, in that the methods outlined here allow such diagrams to be constructed with reasonable speed and facility, as would not have been true a few years ago. The limiting lines L^{pear} and L^{sto}, where the pears and stomatocytes, respectively, attain their fully budded shapes, bound the region where the phase dia-

FIG. 2. Phase diagram of the ADE model for $\alpha = 1.4$. Between the limiting lines L^{pear} and L^{sto} and for reduced volumes $v > 1/\sqrt{2}$, the only equilibrium shapes that appear are pears, prolates, oblates, stomatocytes, and elliptical nonaxisymmtric shapes (nas) with D_{2h} symmetry. Other phases occur outside the limiting lines and for $v < 1/\sqrt{2}$, i.e., in the shaded region. Characteristic equilibrium shapes are illustrated for each phase and for the two limiting lines. First-order, discontinuous transitions (D) are shown as dashed lines; second-order, continuous transitions are shown as full lines. At the special point E, the radii of the two spheres of the limiting pear shape become equal. T_1 and T_2 are tricritical points. The special critical end point CEP is discussed in the text. In the limit $v \to \infty$, the boundaries L^{pear} and $D^{\text{pear/pro}}$ go to plus infinity and the boundaries L^{sto} and $D^{\text{sto/obl}}$ go to minus infinity, as may be shown analytically [7,13]. Locations of the special points are E ($v = 1/\sqrt{2}$), T_1 ($v = 0.730$), T_2 ($v = 0.645$), and CEP ($v = 0.827$). Note the narrow sector where the D_{2h} phase is stable, to the left of CEP between $D^{\text{nas/pro}}$ and $C^{\text{nas/obl}}$.

gram is determined. The region outside these lines is largely "terra incognita" at this time. Studies of the spontaneous-curvature model ($\alpha = 0$) [16] suggest that fully "vesiculated" or "multiplet" shapes, in which two (or more) smooth shapes are connected by one (or more) narrow necks, appear frequently in this region. The region of the full phase diagram at lower reduced volume is much more difficult (and in some sense more interesting), since many other shape classes (including many more nonaxisymmetric shapes) occur. Work is ongoing to sort out this region [26, 27]; however, preliminary indications suggest that it will be difficult with the tools now available and, indeed, that there are many nearby locally stable shapes, so that the usefulness of a theoretical phase diagram in analyzing experiment may turn out in the end to be limited [41].

Above $v = 1/\sqrt{2}$ and in the region between the limiting lines L^{pear} and L^{sto}, the phase diagram involves only five distinct shape classes, the prolates (pro) and oblates (obl) (axisymmetric and with up-down symmetry), the pears (pear) and stomatocytes (sto) (axisymmetric but without up-down symmetry) and a single nonaxisymmetric shape (nas) with the symmetry (D_{2h}) of a rectangular parallelapiped. Transitions between these classes are either discontinuous (dotted lines, notated D) or continuous (full lines, notated C). Three special points appear, two tricritical points (T_1 and T_2, where a first-order transiton becomes second order) and a special kind of critical endpoint (CEP, where a first-order transition disappears, revealing a pair of transitions, one first order and one second order, previously hidden beneath it). The notation $D^{\alpha/\beta}$ or $C^{\alpha/\beta}$ is intended to convey a boundary between the two phases α and β.

Some of the lines shown in Fig. 2 are new to the best of our knowledge; some were previously known. $D^{\mathrm{pear/pro}}$ and $C^{\mathrm{pear/pro}}$ were previously calculated by our group (for $\alpha = 4$) [7]. $D^{\mathrm{sto/obl}}$ and $C^{\mathrm{sto/obl}}$ are new here, as is the prolate/oblate boundary $D^{\mathrm{pro/obl}}$. The transitions into and out of the D_{2h} phase were treated by an approximate, variational method for reduced volume $v = 0.7$ (only) in a recent paper by Heinrich, Svetina, and Žekš [20]. Given here for the first time are exact calculations of $C^{\mathrm{nas/obl}}$ (based on the fluctuation analysis of Sec. II B) and of the full structure, including nonaxisymmetric shapes, at $v = 0.7$ (based on the direct minimization of Sec. II C). Behavior in the vicinity of the critical endpoint is also new. Because the energy of a small neck tends to zero [16], the limiting lines L^{pear} and L^{sto} may be easily found analytically, as was done for the pears in Ref. [7].

All the continuous transitions C can be located, in principle, by the stability analysis outlined in Sec. II B. In practice, however, when both phases are axisymmetric (and the instability appears in the $m = 0$ sector), it is easier to calculate the wing structures, although we have often checked by doing both. The boundary $C^{\mathrm{nas/obl}}$ can only be found via the stability analysis. It occurs in the $m = 2$, even-l subsector. The discontinuous transitions were all calculated by constructing the relevant curves $W^{(n)}(\bar{m}_0)$ for each fixed v and then tracking the intersections as a function of v. This technique fails for $D^{\mathrm{nas/pro}}$,

since one of the two phases is nonaxisymmetric. This boundary is drawn on the basis of knowing exactly the point CEP (see Sec. III D) and having numerical data from our direct minimization approach at $v = 0.7$, as explained in Sec. III C.

It is important to be clear at this point that our work establishes the instability of the prolate and oblate phases towards the D_{2h} shape in a numerically exact manner. On the other hand, we cannot on the basis of the stability analysis alone tell when this instability is a phase boundary and when it is a spinodal. In identifying $C^{\mathrm{nas/obl}}$ as a phase boundary but the prolate instability to D_{2h} as part of the spinodal M^{pro}, we rely on our direct minimization approach [42]. This identification confirms the structure found by Heinrich, Svetina, and Žekš [20] in their approximate calculation.

B. The stability diagram

The stability diagram plots the regions in $(v, \bar{m}_0)$ over which each of the low-lying stationary branches n is locally stable, i.e., the domains where all the physical and non-Euclidean mode energies, $\{\omega^{\alpha}\}$ for $\alpha \in F$, are strictly positive. These regions, which in general overlap, represent the maximum domains of stability and metastability for each branch and include, of course, the corresponding regions of the phase diagram. How much of each metastable region is accessible in the lab depends on how high the energy barriers are that block escape from the local energy minimum. As long as the barriers remain appreciably larger than $k_B T$, metastability will persist. In the vesicle-shape problem, these barriers are generically of order κ, which (as we have discussed in Sec. II) is large on the scale of $k_B T_{\mathrm{room}}$ for common phospholipids. At the boundary of metastability the barrier height shrinks to zero, so, for $T > 0$, a finite unstable band just inside the spinodal boundary is expected.

Figure 3 plots the stability diagram for each of the five stable phases shown in the phase diagram Fig. 2 and over the same region of $(v, \bar{m}_0)$. The overlapping regions of local stability are distinguished by different textures. The boundaries of these regions include the continuous transitions $C^{\alpha/\beta}$ already shown in Fig. 2, the limiting lines L^{pear} and L^{sto}, and, in addition, a set of lines M^{α}, which mark the loci of first soft-mode instability bounding the region where the phase α is metastable.

Every stable phase α is completely surrounded by a stability boundary, which includes the continuous transitions $C^{\alpha/\beta}$, any limiting lines L^{α}, and the instability lines M^{α}. The lines M^{α} are of two types. First, there are the spinodal lines arising from wing structures of the type shown in Fig. 1, where the branch α becomes unstable without any nearby related stable structure. Each spinodal line has been labeled in parentheses by the sector in which the first instability appears. In principle, this sector label can change from one place to another along M^{α}. When the phase α is axisymmetric, this label is m (plus the l parity, when α has up-down symmetry) [43]. Note that, when α becomes unstable at M^{α} and "falls" down to some other locally stable state, there

is no guarantee that that state will be the equilibrium phase immediately adjacent in the phase diagram [44] or even that it will be the ground state appropriate to the local point on the phase diagram (it might be some other metastable state). Knowing what happens after the instability would require doing properly the full dynamics, which is not yet possible even for axisymmetric shapes. The second possibility is that the metastable phase α becomes unstable via a continuous bifurcation of some other branch β of lower energy. We may label the locus of such a bifurcation structure $M^{\alpha/\beta}$, since it is just the analogue of a continuous transition $C^{\alpha/\beta}$, only for a non-ground-state branch. Indeed, if other energy barriers are large, crossing out of the metastable α region via a boundary $M^{\alpha/\beta}$ will appear in the lab to be a smooth shape transformation from branch α to branch β, even though neither α nor β is (strictly) an equilibrium phase at this point.

All the continuous transitions C in Fig. 2 also appear in Fig. 3, as do the tricritical points, T_1 and T_2, and the critical endpoint, CEP, which mark their ends. In addition, two lines, M^α and M^β, emerge from the end of each first-order line $D^{\alpha/\beta}$. Note that part of M^{pro} emerging from T_1 is just a continuation of $C^{pear/pro}$, since in both cases the prolate is becoming unstable to the same $m = 0$, odd-l mode. The situation is slightly different for M^{pear}, since beyond T_1 the pear shapes are no longer up/down symmetric when the instability is reached, so M^{pear} can be labeled only by $m = 0$ but no longer by an l parity.

All metastable boundaries M can in principle be found by searching for soft modes; however, as for the phase diagram, it was usually more convenient to find the $m = 0$ instabilites by studying wing structure. The only lines that cannot be found by the stability analysis are $C^{nas/obl}(m = 2, l$ even), the segment $M^{pro}(m = 2, l$ even) emerging from CEP to the left, and M^{nas}. For the particular case of $v = 0.7$, we have determined the location of these points by using direct energy minimization (see Sec. III C). Previous to this work, the only spinodal explicitly calculated was the segment of M^{pro} emerging from T_1.

C. Direct minimization for $v = 0.7$

In this section, we present results obtained by directly minimizing the bending energy, Eq. (8), on a triangulated surface, as described in Sec. II C. Since this method is quite time consuming if high precision is required, we have chosen to calculate only one representative cut through the phase diagram, at $v = 0.7$. Figure 4 shows the energies of the oblate, prolate, and D_{2h} branches as functions of the area difference $\bar{m}_0$ for $\alpha = 1.4$.

As $\bar{m}_0$ is increased, the oblates undergo a continuous transition $C^{nas/obl}$ to D_{2h} shapes at about $\bar{m}_0 = 1.08$, which should be compared with $\bar{m}_0 = 1.079$, as obtained from the stability approach. Similarly, the prolate branch becomes unstable at the spinodal M^{pro} at $\bar{m}_0 = 1.10$, compared with the value $\bar{m}_0 = 1.097$ obtained from the stability analysis. The nonaxisymmetric branch exhibits
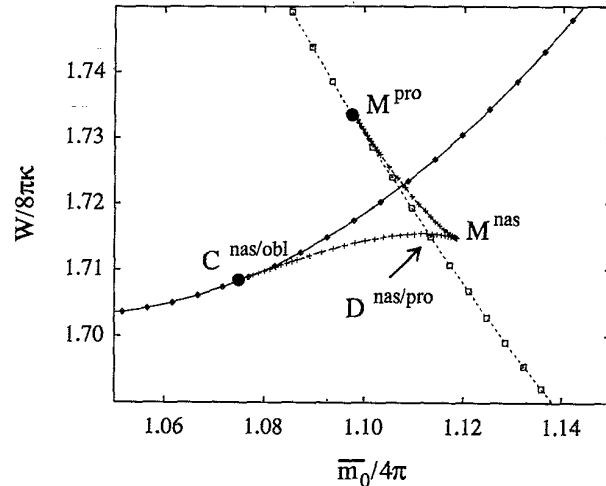

FIG. 4. Energies $W^{(n)}$ of prolates (squares) oblates (diamonds), and nonaxisymmetric ellipsoids (crosses) as a function of area difference $\bar{m}_0$ at $v = 0.7$, as obtained from direct minimization. Unstable oblates show up to the right of the bifurcation at $\bar{m}_0 = 1.08$, whereas unstable prolates show up to the left of the bifurcation at $\bar{m}_0 = 1.10$. Note the structures corresponding to the special points M^{pro}, M^{nas}, $C^{nas/obl}$, and $D^{nas/pro}$.

a wing structure, which leads to a first-order transition $D^{nas/pro}$ at $\bar{m}_0 = 1.11$. For the activation energy at the transition, we find the small value 0.06κ, which corresponds roughly to $k_B T$ for SOPC near room temperature. The nonaxisymmetric branch becomes unstable at the cusp, where $\bar{m}_0 = 1.12$. These numbers are in excellent agreement with those obtained by Heinrich et al. in Ref. [24] (Fig. 7), suggesting that their approximate calculation is quite accurate in this regime.

The numerical uncertainties in the values of $\bar{m}_0$ derived from the mapping described in Sec. II A are of the order of 10^{-2}. They are mainly caused by uncertainty in $\partial G^{(n)}(m)/\partial m$, which has to be calculated numerically along the nonaxisymmetric branch from the results of the minimization at $\alpha = \infty$. Compared to that uncertainty, the numerical error in m at the two bifurcations, which is of the order of 10^{-3}, is negligible.

The fact that both the oblate and the prolate branches are displayed beyond the bifurcation in Fig. 4 may look surprising, given the fact that such shapes are also unstable for $\alpha = \infty$. These shapes and their energies have been obtained by using nearby locally stable axisymmetric shapes to initialize the numerical minimization routine. The minimization will detect an unstable mode only if the initial shape contains some minimum nonzero contribution of that mode. It turns out that, for the axisymmetric shapes beyond the bifurcation, this requirement in practice is not fulfilled. Of course, if the axisymmetry is broken by hand in the initial shape, the minimization will find the true nonaxisymmetric minimum.

D. Bifurcation structures

The various phase transitions and spinodals in Figs. 2 and 3 arise from structures in the overall energy dia-

gram $\{W^{(n)}(\bar{m}_0)\}$ for that set of stationary branches n that have locally stable domains. A simple crossing of distinct branches involving the lowest energy levels produces a first-order transition D; a tangent bifurcation of the lowest level produces the continuous transitions C; and, a spinodal line M can come from either a wing structure like Fig. 1 or a bifurcation in a non-ground-state level. What is more interesting is the interrelation between these structures, which occurs in the neighborhood of the tricritical points T and the critical endpoint CEP.

The points $T \equiv ((\bar{m}_0)_T, v_T)$ lie on a boundary between an up-down symmetric phase (the prolate or the oblate) and a phase in which this symmetry has been broken (while still maintaining axial symmetry). The bifurcation structure around these two points is represented locally by a Landau theory of the form

$$V[\phi] - W_B = -\frac{1}{2}r\phi^2 - \frac{1}{4}g\phi^4 + \frac{1}{6}u\phi^6. \tag{31}$$

The lowest energy of the functional $V[\phi]$ gives the free energy of the equilibrium state near the point T. Here, ϕ represents the amplitude of the principle physical (i.e., volume and area preserving) mode, which breaks the up-down symmetry. W_B is the "background" energy coming from modes that are nonsingular at T, so it depends smoothly on the phase-diagram variables $(v, \bar{m}_0)$ and gives the full ground-state energy at T and wherever $\phi = 0$ at equilibrium. g and r are distances in the phase diagram from the point T measured, respectively, along the line C/D and perpendicularly to it. At lowest order, they are both just appropriate linear combinations of $v - v_T$ and $\bar{m}_0 - (\bar{m}_0)_T$. For the prolate-pear boundary, as shown in Fig. 2, g would be roughly proportional to $v - v_T$ and r, to $\bar{m}_0 - (\bar{m}_0)_T$; for the oblate-stomatocyte boundary, the sign of r would be reversed. u depends on v and $\bar{m}_0$ but is generically positive. In terms of these scaling variables, it is easy to calculate explicity the phase boundaries and spinodals, as shown in Fig. 5 (labeling has been done to conform generically to the pear-prolate boundary). Note that the $D^{\mathrm{pear/pro}}$, M^{pro}, and M^{pear} emerge from T parallel to one another and to the direction of $C^{\mathrm{pear/pro}}$. Also sketched as insets in Fig. 5 are representative curves $(W - W_B)(r)$ for typical values of $g < 0$ and $g > 0$, showing the characteristic bifurcation structure.

Figure 6 shows in blown-up form a semischematic view of what goes on along the prolate-oblate phase boundary and its continuation beyond the special point CEP to lower reduced volumes, where a narrow wedge of nonaxisymmetric equilibrium shapes (D_{2h}) first appears. Corresponding constant-v sections through the full energy diagram are sketched in Fig. 7 to illustrate the bifurcation structures. The two roughly parabolic curves represent the energies of the prolate and oblate stationary branches, which are always the equilibrium shapes at sufficiently large $\bar{m}_0$ and sufficiently small $\bar{m}_0$, respectively. At high reduced volume (slice No. 1), these two curves simply cross, producing the first-order transition $D^{\mathrm{pro/obl}}$. The crucial feature of the structure, visible in Fig. 7 and first discovered by Heinrich, Svetina, and Žekš
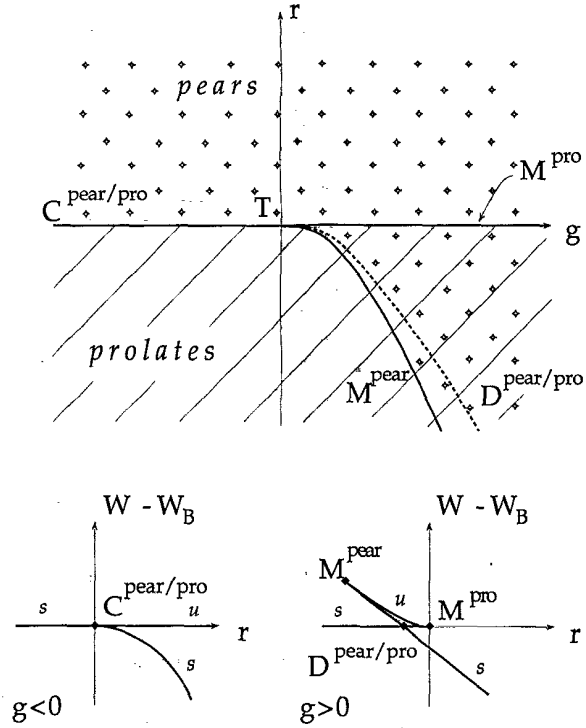

FIG. 5. Phase diagram and stability diagram of the Landau theory described by Eq. (31). Note the tricritical point T separating the continuous transition C and the discontinuous transition D. The spinodal lines M mark the limits of metastability of the corresponding phases. Note how the first-order line D lies in the region in which both the coexisting phases are locally stable. All boundaries are horizontal where they meet at T in these (scaling) variables. Sections $W(r)$ of the corresponding energy surface are shown below for $g < 0$ and $g > 0$. Stable (s) and unstable (u) branches are labeled.
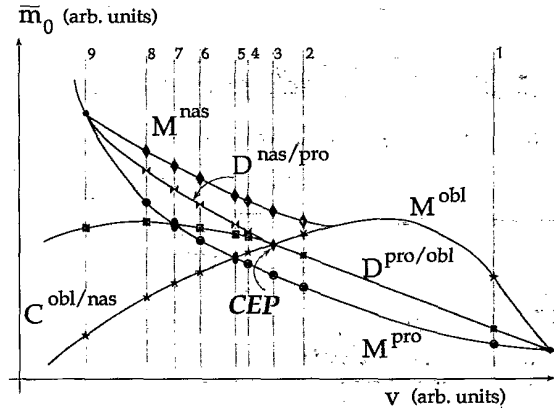

FIG. 6. Schematic representation of the phase diagram (filled symbols) and other structures (open symbols), including the spinodals M, along the oblate-prolate boundary and in the vicinity of the CEP. The symbols are keyed to the generic energy diagrams displayed in Fig. 7. The axes here are not to scale but the interconnections between the various lines are given correctly. This region is shown in Figs. 2 and 3; but, the scale there does not allow the interrelation between the various lines to be seen. Note the crossing of M^{obl} and M^{pro}, which takes place to the left of the CEP at $v = 0.684$. In the region between the two spinodals to the left of this point, no axisymmetric shapes are locally stable.

[20], is the presence of the low-lying branch of nonaxisymmetric stationary shapes which bifurcates from and smoothly connects the prolate and oblate branches. At high enough v, this branch is entirely unstable; however, below a certain reduced volume a wing structure develops at the point where this branch bifurcates from the oblate branch, and the structure becomes that shown in slice No. 2. All this occurs initially in nonequilibrium branches of the stationary energies, and the local bifurcation structure is exactly as shown in Fig. 5, only with various signs reversed. At the critical endpoint CEP (slice No. 3), this bifurcation first emerges from beneath the prolate energy and translates into a closely spaced second-order transition ($C^{nas/obl}$) and first-order transition ($D^{nas/pro}$) [45]. The crossing shown in Fig. 6 between the prolate and oblate spinodals occurs at slice No. 5 but has no significance for the phase diagram, since the prolate at this point is a high-energy branch. At reduced volumes lower than that of the CEP, the first-order boundary $D^{nas/pro}$ lies between $M^{pro}(m = 2, l$ even) (below) and M^{nas} (above), as shown in our numerical data, Fig. 4. It is conjectured that, beyond a certain reduced volume (slice No. 9), the wing structure where the D_{2h} branch bifurcates from the prolate disappears, so that $D^{nas/pro}$ and M^{nas} merge with $M^{pro}(m = 2, l$ even) at another tricritical point and the nas/prolate instability

continues to lower reduced volume as $C^{nas/pro}$. From our direct-minimization work, we know that the reduced volume at which this could happen is bounded above by $v = 0.7$.

IV. SUMMARY

Between the limiting lines L^{pear} and L^{sto}, which mark vesiculation boundaries and in the region of relatively high reduced volumes, $v \geq 1/\sqrt{2}$, vesicle shapes are dominated by five shape classes, four of which are axisymmetric (pears, prolates, oblates, stomatocytes) and one of which is not (D_{2h}). This statement is true for values of the parameter $\alpha = \bar{\kappa}/\kappa$ (which measures the ratio of the nonlocal and local bending constants) of order unity [46]. By exploiting our ability to calculate the energies and stability of these axisymmetric shapes, we can explicitly construct most (but not quite all) of the phase boundaries and spinodal lines in this region. Additional required information related to the nonaxisymmetric shapes has been obtained by employing a direct minimization routine. The phase diagrams and metastability lines we have produced (Figs. 2 and 3) refer to a value, $\alpha = 1.4$, appropriate to SOPC; however, providing comparable information for any other value would now be straightforward. Many but by no means all interesting experiments and
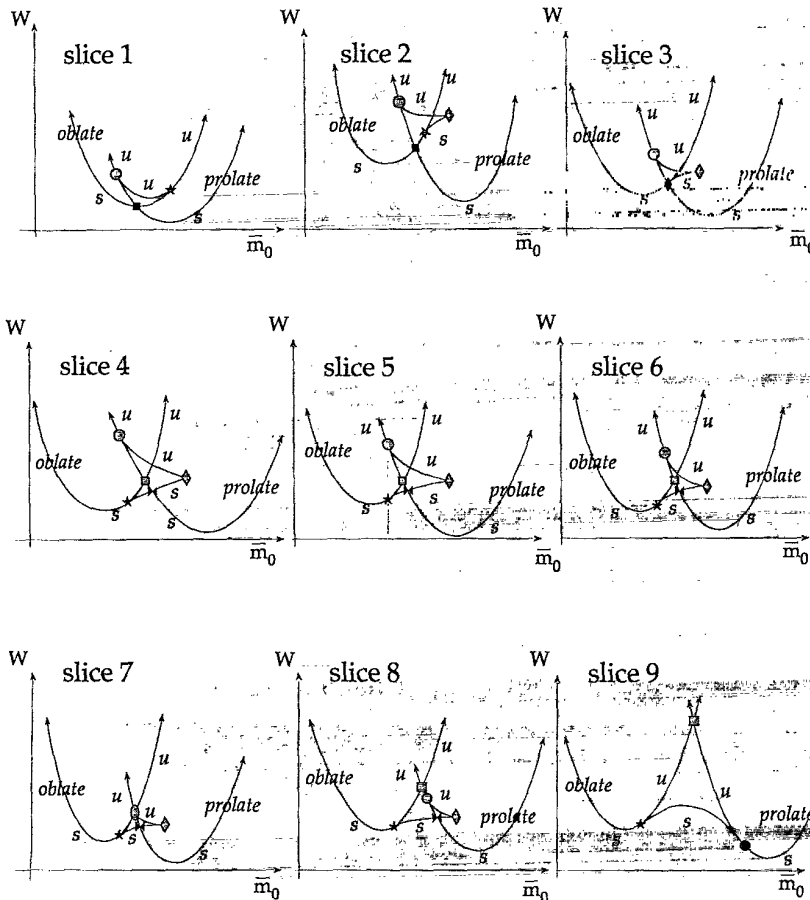

FIG. 7. Schematic representation of the energies of the stationary-shape branches along the cuts labeled in Fig. 6. Stable (s) and unstable (u) branches are labeled. The symbols which mark the various level crossings, wings, and bifurcations correspond to those marking the curves in Fig. 6. Stationary oblate and prolate shapes occur along the two roughly parabolic intersecting curves in each figure. Bifurcating from these branches and connecting them is the D_{2h} branch of nonaxisymmetric (nas) stationary shapes. In slice No. 1, all these nas shapes are locally unstable; in slice No. 9, they are all locally stable. Between these limits, the nas branch displays a wing structure at which the local stability changes. The lowest-energy shape at each value of $(v, \bar{m}_0)$ is the (stable) equilibrium shape. The CEP occurs at slice No. 3. At slice No. 5, the spinodals M^{obl} and M^{pro} cross.

applications lie in this region. We hope that the existence of a theoretical framework which makes one-parameter (α) predictions [47] for locally stable vesicle shapes (and thermal fluctuations around them) in this region will be an incentive to experimentalists.

Many experimentally observable and conceptually interesting shapes lie outside of this regime, at low reduced volumes and in the vesiculated regions. These include a wide range of branched, tubular, and multiplet structures. The theory will be harder to control in these sectors, which are not dominated by simple axisymmetric shapes. Some progress can be made by numerical methods [26, 27]; but, convergence of theory and experiment in this wider arena remains a significant challenge to both.

ACKNOWLEDGMENTS

[1] E. Sackmann, H.P. Duwe, and H. Engelhardt, Faraday Discuss. Chem. Soc. 81, 281 (1986).

[2] E. Evans and W. Rawicz, Phys. Rev. Lett. 64, 2094 (1990).

[3] K. Berndl, J. Käs, R. Lipowsky, E. Sackmann, and U. Seifert, Europhys. Lett. 13, 659 (1990).

[4] J. Käs and E. Sackmann, Biophys. J. 60, 825 (1991).

[5] R. Lipowsky, Nature (London) 349, 475 (1991).

[6] E. Farge and P. Deveaux, Biophys. J. 92, 347 (1992).

[7] L. Miao, U. Seifert, M. Wortis, and H.-G. Döbereiner, Phys. Rev. E 49, 5389 (1994), contains additional references.

[8] H.-G. Döbereiner, Ph.D. thesis, Simon Fraser University, 1995 (unpublished).

[9] H.G. Döbereiner, E. Evans, U. Seifert, and M. Wortis, Phys. Rev. Lett. 75, 3360 (1995).

[10] H.J. Deuling and W. Helfrich, J. Phys. (Paris) 37, 1335 (1976).

[11] P.B. Canham, J. Theor. Biol. 26, 61 (1970).

[12] W. Helfrich, Z. Naturforsch. 28c, 693 (1973).

[13] U. Seifert, K. Berndl, and R. Lipowsky, Phys. Rev. A 44, 1182 (1991).

[14] H. Hotani, J. Mol. Biol. 178, 113 (1984).

[15] W. Wintz, H.-G. Döbereiner, and U. Seifert (unpublished).

[16] L. Miao, B. Fourcade, M. Rao, M. Wortis, and R.K.P. Zia, Phys. Rev. A 43, 6843 (1991).

[17] B. Fourcade, L. Miao, M. Rao, M. Wortis, and R.K.P. Zia, Phys. Rev. E 49, 5276 (1994).

[18] S. Svetina, M. Brumen, and B. Žekš, Stud. Biophys. 110, 177 (1985).

[19] S. Svetina and B. Žekš, Eur. Biophys. J. 17, 101 (1989).

[20] V. Heinrich, S. Svetina, and B. Žekš, Phys. Rev. E 48, 3112 (1993). This paper treats $v = 0.70$, 0.85, and 0.95 (only) but for a range of α.

[21] S. Svetina, A. Ottova-Lietmannová, and R. Galser, Theor. Biol. 94, 13 (1982); S. Svetina and B. Žekš, Biome. Biochim. Acta 42, S86 (1983); 44, 979 (1985).

[22] U. Seifert, Z. Phys. B 97, 299 (1995).

[23] M. Jarić, U. Seifert, and M. Wortis (unpublished).

[24] V. Heinrich, M. Brumen, R. Heinrich, S. Svetina, and B. Žekš, J. Phys. (France) II 2, 1081 (1992).

[25] The equations themselves have been written down by Ou-Yang Zhong-can and W. Helfrich, Phys. Rev. Lett. 59, 2486 (1987).

[26] W. Schnitzler (now: W. Wintz), Diplomarbeit, RWTH Aachen, 1993 (unpublished).

[27] W. Wintz and U. Seifert (unpublished).

[28] An irrelevant topological term associated with the local Gaussian curvature has been omitted.

[29] The origin ΔA_0 is the different number of lipid molecules in the inner and outer leaves of the bilayer and the fact that this difference relaxes slowly on mechanical time scales. See Ref. [7].

[30] For a pure spontaneous-curvature (SC) model with a reduced spontaneous curvature $\bar{c}_0$, for which only the first term of Eq. (1) occurs, it is easy to show that the variational equation takes the form

$$\delta F = \kappa \left(\delta G[S] - 2\bar{c}_0 \delta m[S] \right) = 0.$$

It follows immediately that the shape S that solves Eq. (11) is also a stationary shape of a pure spontaneous curvature model with spontaneous curvature

$$\bar{c}_0 = \frac{\alpha}{2}(\bar{m}_0 - m[S]).$$

[31] Note from Ref. [30] that $\partial G^{(n)}/\partial m$ is just twice the reduced spontaneous curvature $\bar{c}_0$ of the corresponding SC model.

[32] Reference [22] focuses on computing the thermal fluctuations and implements the constraints as strict delta functions inside the appropriate partition function. Here, we focus principally on the spectrum and are led to implement the constraint projections.

[33] M. Peterson, J. Math. Phys. 26, 711 (1985); J. Appl. Phys. 57, 1739 (1985); M. Peterson, H. Strey, and E. Sackmann, J. Phys. (France) II 2, 1273 (1992).

[34] We follow the sign conventions of Ref. [22]. In Ref. [22], the stability matrix is denoted S_{ij}.

[35] In principle, the constraint space might turn out to be of dimension less than two, which would require minor modifications of what follows. In practice, this does not happen.

[36] Note that this condition forces a particular choice of axes on shape experiments that would make contact with the theory.

[37] The thermal shifts as given here might be modified, if nontrivial measure factors become relevant, such as the

Liouville factor discussed in W. Cai, T. Lubensky, P. Nelson, and T. Powers, J. Phys. (France) II **4**, 931 (1994). See the comments in Appendix A of Ref. [22].

[38] U. Seifert, Habilitation thesis, Ludwig-Maximilians-Universität München, 1995 (unpublished).

[39] K. Brakke, Experimental Math. **1**, 141 (1992).

[40] R. Waugh, J. Song, S. Svetina, and B. Žekš, Biophys. J. **61**, 974 (1992).

[41] In such a situation, an extended stability diagram, showing the overlapping regions of local stability of the various coexisting shapes would still be useful, as would predictions of postinstability destinations.

[42] Certain inferences are possible, based on the lines we do control. For example, as long as $M^{\mathrm{pro}}(m = s, l$ even) remains below (in $\bar{m}_0$) the continuation of $D^{\mathrm{pro/obl}}$ (shown in Fig. 6) it must be higher in energy than $W^{(\mathrm{obl})}$, so the phase boundary nas-pro certainly cannot be second order for reduced volumes between this point and the CEP.

[43] Note, of course, that in any nas phase these labels no longer apply.

[44] An example is thermally induced budding out of the prolate phase, which commonly leads to a vesiculated shape rather than to one in the adjacent pear phase. See Refs. [7–9].

[45] Note how $D^{\mathrm{nas/pro}}$ emerges from the CEP parallel to $D^{\mathrm{pro/obl}}$ because of the bifurcation structure at $M^{\mathrm{obl}}(m = 2, l$ even), where $W^{(\mathrm{obl})}(\bar{m}_0)$ and $W^{(\mathrm{nas})}(\bar{m}_0)$ are locally parallel.

[46] It is probably also valid beyond this region, except possibly for very high values of α, where the nonaxisymmetric region penetrates close to $v = 1$. See Ref. [13].

[47] Of course, α is in principle measurable in experiments like those of Ref. [40], so in this sense the theory is zero parameter. In practice, the difficulty in comparing theory and experiment is usually the fact that $\bar{m}_0$ is not directly accessible to experiment. A technique for handling this difficulty is discussed in Ref. [8].